Nuclear Instruments and Methods in Physics Research A 1064 (2024) 169438

Contents lists available at ScienceDirect

Nuclear Inst. and Methods in Physics Research, A

journal homepage: www.elsevier.com/locate/nima

Full Length Article

Enabling pulse shape discrimination with commercial ASICs

John Leland [a], Ming Fang [a], Satwik Pani [a,b], Yuri Venturini [c], Marco Locatelli [d], Angela Di Fulvio [a,*]

[a] Department of Nuclear, Plasma, and Radiological Engineering, University of Illinois, Urbana-Champaign, 104 South Wright Street, Urbana, IL 61801, United States

[b] Department of Radiation Oncology, Washington University School of Medicine, 660 S. Euclid Ave, St., Louis, MO, 63110, United States

[c] CAEN SpA, Via della Vetraia 11, Viareggio, 55049, Italy

[d] CAEN Technologies Inc., 1 Edgewater Street - Suite 101 Staten Island, NY 10305, United States

ARTICLE INFO

Keywords:
Silicon photomultiplier
Pulse shape discrimination
Application specific integrated circuit

ABSTRACT

Fast electronic readout for high-channel density scintillator-based systems is needed for radiation tracking and imaging in a wide range of applications, including nuclear physics, nuclear security and nonproliferation. Programmable electronics, like FPGAs and ASICs, provide a fast way of conditioning and processing the signal in real time. In this paper, we present a pulse shape discrimination (PSD) method based on the shaping circuit of a commercially available ASIC, the Citiroc1A by CAEN Technologies. We used two different shaping times per detector channel to calculate a shaping parameter that enables PSD. Using our new method, neutron and gamma-ray pulses detected by a d_{12}-stilbene scintillator can be effectively discriminated at light output values greater than 0.15 MeVee. While not achieving the PSD performance of traditional offline charge integration, our method does not require the transfer of data to a separate system for further processing and enables the direct deployment of high-channel density multi-particle detection systems. Moreover, the availability of a wider range of shaping times than those on the Citiroc1A can potentially further improve the PSD performance.

1. Background and motivation

The availability of solid-state light readout devices, like silicon photomultipliers (SiPMs), makes it possible to scale large arrays of scintillation detectors [1,2] to hand-held versions [3,4]. Compared to avalanche photo-detectors and photo-diodes, SiPMs exhibit better performances, e.g., higher gain, lower noise, and a faster response [5]. When SiPMs are coupled with pulse-shape discrimination (PSD) capable scintillators, they allow for the simultaneous detection of different types of radiation, e.g., gamma rays and neutrons. Furthermore, the advantage of using SiPMs is the ability to handle a high number of channels, in the order of hundreds, while maintaining a compact form factor, ideal for hand-held stand-off gamma ray and neutron imaging. Programmable electronics, like field programmable gate arrays (FPGA) and application specific integrated circuits (ASICs), are particularly suitable for the readout of SiPMs coupled to arrays of scintillation detectors because they can perform similar complex functions as traditional analog electronics [6] and fast digitizers [7] while being compact and featuring a high number of channels. However, implementing specific functions, such as PSD, requires the design of custom ASIC-based devices, which are cost prohibitive for small-scale projects.

In this work, we address this issue by developing a method to perform PSD using the commercially available Citiroc1A ASIC controlled by the A55CIT4-DT5550W readout system [8,9] by CAEN Technologies (Viareggio, Italy). This PSD method does not require sampling and storing hundreds of samples for each detected pulse, which corresponds to the analog-to-digital conversion process implemented on fast digitizers. Additionally, our method can be performed on-board without the need of transferring the data to another device for analysis.

The ASIC-based method implements an architecture that extracts a pulse-shape-dependent parameter, which enables the discrimination of gamma-ray and neutron pulses. In the 70 s, similar analog PSD methods were explored and implemented. These methods typically perform PSD using a shaping stage followed by a time-to-amplitude circuit and comparator that discriminates between neutron and gamma-ray pulses [10,11]. While being inspired by the analog implementation, our method expands on the prior work by translating the analog architectures to digital processing and enables PSD for high-channel density detector arrays using advanced on-board signal processing. Therefore, the method we propose grants the capability to perform PSD on a compact detection system with a high number of channels for a broad range of applications, including nonproliferation, nuclear physics, and radiation protection.

We developed and implemented an on-board PSD method for the commercially available Citiroc1A ASIC [12]. In Section 2, we introduce

* Corresponding author.
E-mail address: difulvio@illinois.edu (A. Di Fulvio).

https://doi.org/10.1016/j.nima.2024.169438
Received 15 February 2024; Received in revised form 2 May 2024; Accepted 9 May 2024
Available online 13 May 2024

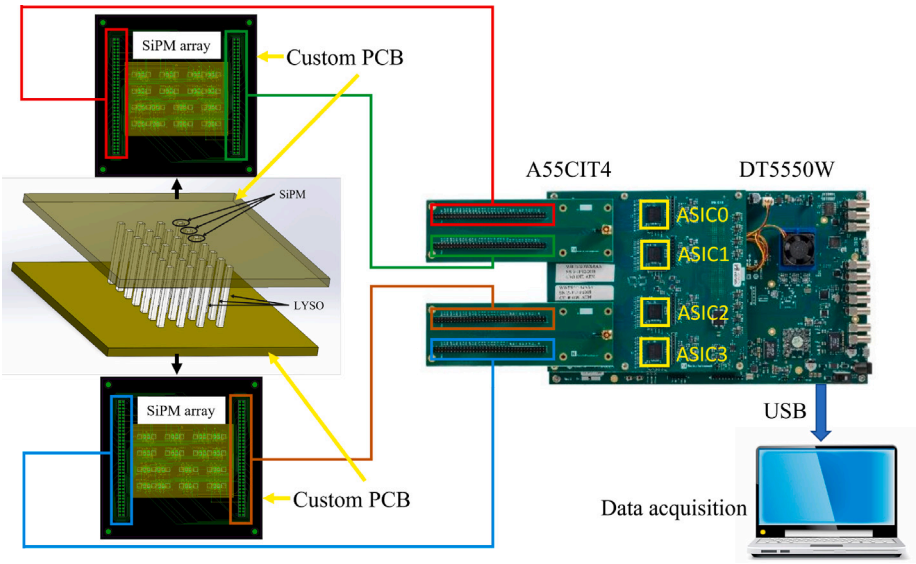

Fig. 1. Schematic of a multi-particle spectroscopic imager based on an ASIC-based electronic readout.

the ASIC-based method, which we will call Digital Shaper (DS) PSD, to discriminate between neutron and gamma-ray pulses and calculate the circuit response function for optimizing the PSD parameter using template pulses. In Section 3, we apply the optimized PSD method on measured gamma-ray and neutron pulses. A comparison between the traditional charge-integration (CI) PSD and DS PSD is given. The discussion and conclusions are presented in Section 4

2. Methods

In this section, we describe the implementation of PSD using electronics available in the Citiroc1A ASIC. The DS PSD method will be demonstrated on synthetic pulses and experimentally measured data, and its performance will be compared with the traditional PSD method.

2.1. Imaging system design

We built a compact imaging system encompassing a 4 × 7 array of LYSO crystals (3 mm×3 mm×5 cm) coupled to 56 Onsemi MicroFJ 30020 SiPMs [13] that are read out by four Citiroc1A ASICs. In the future, the LYSO will be replaced by PSD-capable scintillators such as stilbene. This detector can be used as an imager for nuclear security and non-proliferation applications and as a particle tracker for nuclear physics experiments. Fig. 1 shows the schematic of the imager. The system includes two custom-printed circuit boards (PCBs), each powering and controlling the readout of a 4 × 7 array of SiPMs. The SiPM arrays are used for light readout of the top and bottom sides of a 4 × 7 scintillator matrix. The dual-end readout enables the retrieval of depth of interaction information [14,15]. The SiPM pulses are fed to an A55CIT4-DT5550W readout system by CAEN Technologies [9]. The system is controlled via computer using the DT5550W Readout Software (Sci Digitizer Family, Version 2022.1.1.0, distributed by CAEN Technologies). This software allows us to control the DT5550W and program some of the board settings, including the gain, the threshold, and the shaping constants. The A55CIT4 board hosts four Citiroc1A ASICs, each with a 32 readout channel capacity [8]. Thus, there are 128 input channels available in total. This board is particularly suitable for SiPM readout because it provides a bias from 20 V to 85 V with a current up to 10 mA [16]. In the current configuration, the board is set to provide a 30 V bias to the SiPMs. The A55CIT4 board features a fine time resolution better than 100 ps as stated by the manufacturer [8] and a 14-bit ADC with a sensitivity of 160 fC. We tested the effect of the Citiroc1A's dead time on our data throughput using the DT5810B pulse generator. We found no loss of data when up to a 10 kHz input frequency. This acquisition rate is compatible with the detection of an approximately 6 mCi source at a distance of 1 m with our imager without. Therefore, the proposed configuration is suitable for imaging applications, even when measuring relatively high-intensity sources.

2.2. PSD method

In this section, we briefly summarize the principles of two PSD methods, namely the traditional charge-integration PSD and the proposed DS PSD. The datasets used for the evaluation of the PSD methodologies are:

A. Synthetic dataset acquired using a pulse generator connected to the ASIC.
B. Measured waveform dataset produced using a stilbene-d_{12} crystal, SiPM evaluation board, and DT5730 digitizer.
C. Measured dataset produced using a stilbene-d_{12} crystal, SiPM evaluation board, and Citiroc1A ASIC.

2.2.1. Charge-integration PSD

PSD-capable scintillators emit blue-UV light upon interaction with ionizing radiation through prompt and delayed fluorescence [17]. In organic scintillators, the light-emitting molecular excitation reactions are mainly due to recoil protons and electrons, produced by neutron and gamma-ray collisions, respectively. For an equivalent deposited energy, recoil protons produce a higher amount of delayed fluorescence, compared to electrons, due to their higher ionization density, which results in a larger delayed component in the detected pulses [17,18]. This difference in delayed components can then be used to discriminate between gamma-ray and neutron pulses. Figure set 2 shows the procedure to obtain the template pulses. Figs. 2(a) and 2(b) show the measured gamma-ray and neutron pulses averaged over 0.2 MeVee-wide bins from 0.1 MeVee to 1.7 MeVee. Figs. 2(c) and 2(d) are these pulses normalized to their respective peak values. Fig. 2(e) shows the template gamma-ray and neutron pulses, which are the normalized pulses averaged over the entire light output range. The difference between the delayed fluorescence component of gamma-ray and neutron-induced pulses is clearly visible.

Traditionally, charge integration (CI)-based PSD [19] is used to perform PSD. CI takes advantage of the difference in delayed components by defining the PSD parameter as the ratio of the area under the pulse tail to the total area (tail-to-total ratio) of the measured pulse, as shown

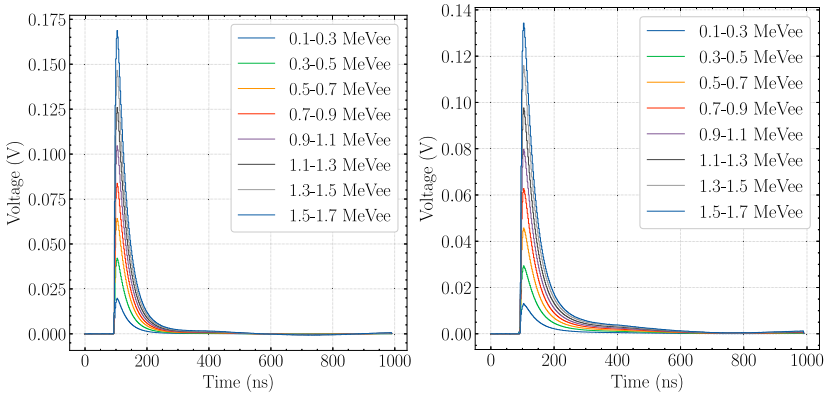

(a) Average gamma-ray pulses. (b) Average neutron pulses.

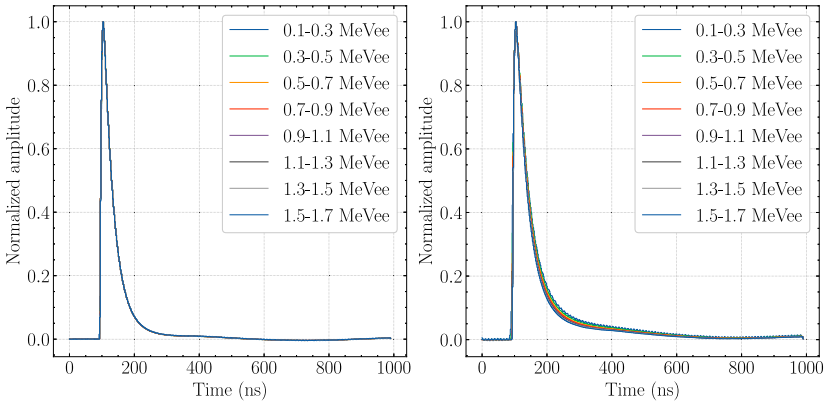

(c) Normalized average gamma-ray pulses. (d) Normalized average neutron pulses.

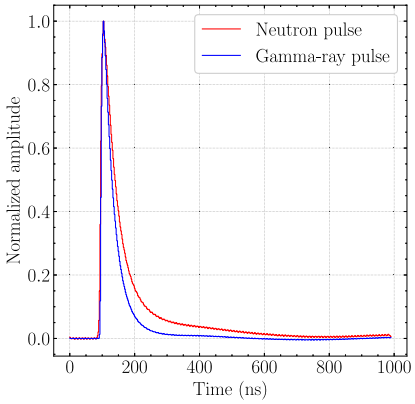

(e) Templates created by averaging pulses in entire light output range.

Fig. 2. Normalized neutron and gamma-ray template pulses acquired by measuring a ^{239}PuBe source with a stilbene-d$_{12}$ crystal.

by Eq. (1). The pulses are measured in voltages as designated by $V(t)$ and t_0 is the beginning of the pulse, t_1 is on the falling edge of the pulse, and t_2 is the end of the pulse.

$$\mathrm{PSD_{CI}} = \frac{\sum_{t_1}^{t_2} V(t)}{\sum_{t_0}^{t_2} V(t)} \tag{1}$$

Neutron pulses exhibit higher tail-to-total ratios due to the larger delayed components, which enable their discrimination from gamma-ray pulses.

2.2.2. Digital shaper PSD

The Citiroc1A front-end encompasses a readout circuit with two independent paths, referred to as the low-gain (LG) and high-gain (HG) path. Each path consists of a low-gain/high-gain charge preamplifier, a pulse shaper, and a peak sensing circuit that detects and records the maximum of the shaped signal [8], as shown in Fig. 3. Since gamma rays and neutrons have different pulse shapes, they exhibit different responses to the shaper in the Citiroc1A. It is therefore possible to perform PSD based on this difference in the shaper's responses.

For this method, the PSD parameter is defined as the ratio between the HG and LG output signals as shown by Eq. (2). The two paths of the readout circuit are linear with energy, as shown in the manual[1] [20]. Therefore, the PSD parameter is mainly a function of

[1] The manual refers to the Citiroc-1A chip being controlled by the A5202/DT5202 module. While the control module is different, the Citiroc-1A is the same used in this work. Therefore, the linearity of the acquisition chain, shown in section 9.2.3 of the manual, applies to our work.

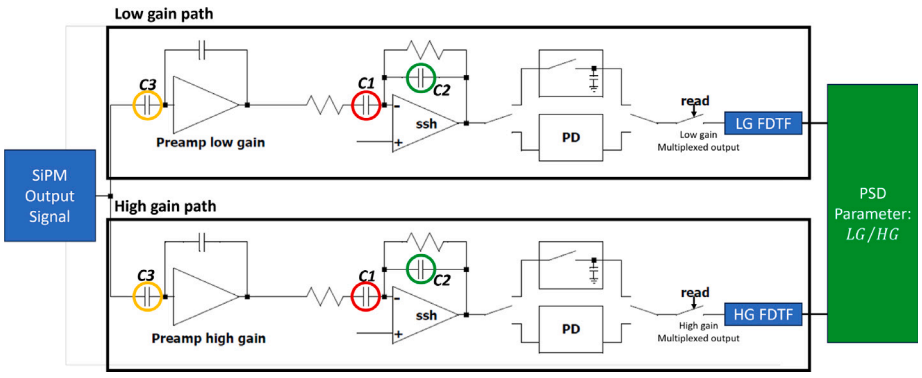

Fig. 3. Calculation of the PSD parameter based on LG and HG outputs. SSH is the slow shaper and PD is the Peak Detector circuit [8].

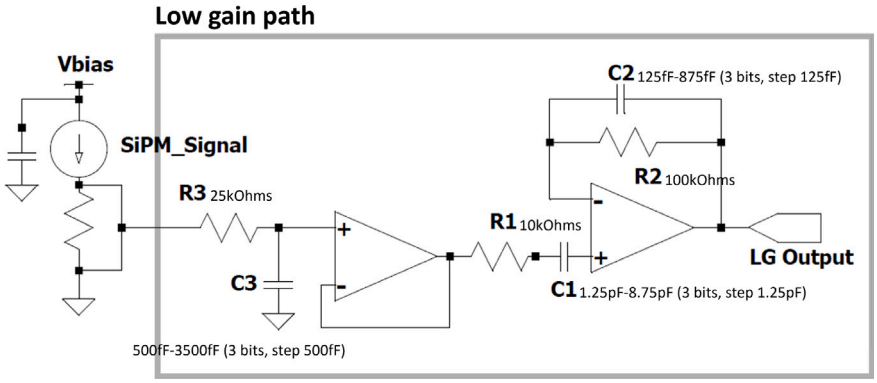

Fig. 4. Single channel pulse shaper on the Citiroc1A. C1, C2, and C3 are the capacitances controlled by the peak time [12].

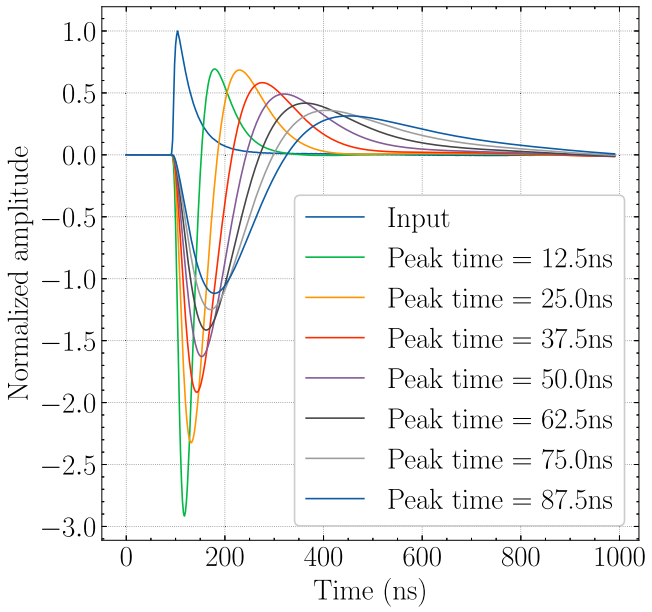

Fig. 5. Signals output by FDTF with different peak times.

the pulse shape with a slight dependence on the pulse height. Fig. 3 illustrates the steps needed to calculate the PSD parameter. The pulse shaper is shown in Fig. 4. Its response is dependent on a set of three adjustable capacitances — C_1, C_2, C_3 — also shown in Fig. 3. These capacitances are controlled through the "peak time" setting in the readout software. There are a total of seven available peak times each associated with a specific set of capacitances. To achieve the best PSD performance, we optimized the values of C_1, C_2, and C_3 to maximize the difference in PSD parameters of neutron and gamma-ray pulses. A detailed description of the optimization method is in the following Section 2.3.1.

$$\mathrm{PSD_{ASIC}} = \frac{\text{HG output}}{\text{LG output}} \tag{2}$$

2.3. Computational implementation of DS PSD

In this section, we calculate the response of the ASIC's acquisition chain, based on which we can determine the optimal ASIC settings for PSD.

2.3.1. Transfer function and pulse shape

The response of the front-end acquisition chain of the ASIC was calculated based on the known architecture. A set of template gamma-ray and neutron pulses, shown in Fig. 2(e), were used to test the response of the front-end to prototypical pulses. The template neutron and gamma-ray pulses were obtained by averaging 10,000 neutron and gamma-ray pulses, respectively, and normalizing them to the single pulse maximum value. The experimental method used to obtain these pulses is described in Section 2.4 in greater detail.

We calculated the frequency-dependent-transfer-function (FDTF) of the pulse shaper (Fig. 4) in the Laplace domain, shown by Eq. (3). f stands for the frequency and $T(s)$ is the ratio between the output signal and input signal. C_1, C_2, and C_3 are the capacitances controlled by the peak time setting in peak sense mode of the readout software and the set relationship between the peak times and capacitances is shown in Table 1. The capacitances and R_1, R_2, and R_3 are shown in Fig. 4 as

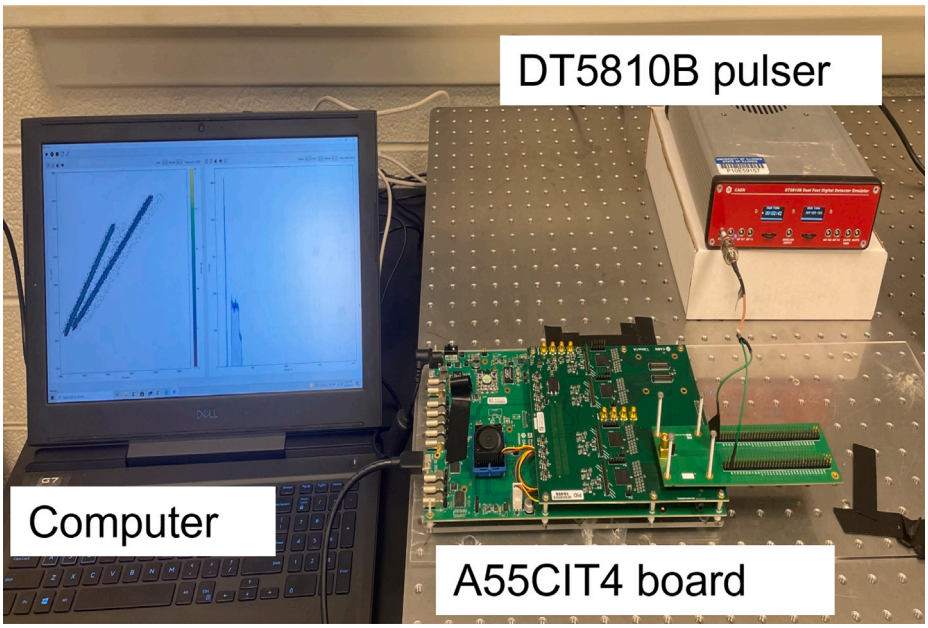

Fig. 6. Emulated pulses experimental setup. The pulse generator output is connected directly to the ASIC and the output is recorded and processed in real-time by the computer to perform PSD.

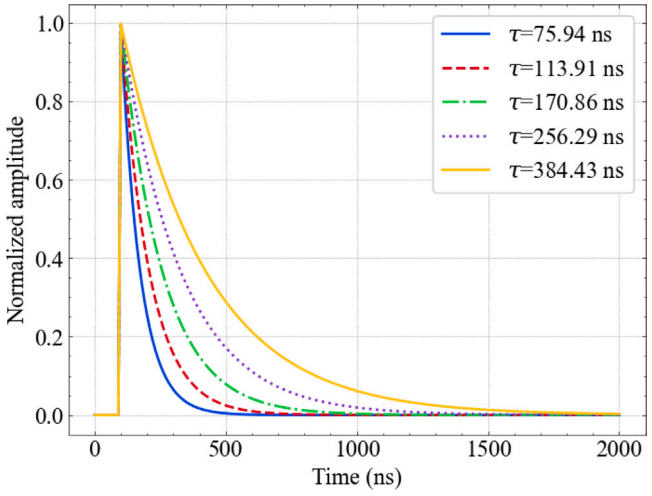

Fig. 7. Normalized measured emulator pulses.

well. The resistive values are specific to the ASIC itself and cannot be tuned by the user via software.

$$T(s) = \left(\frac{1}{sR_3C_3 + 1}\right)\left(\frac{s^2R_1C_1R_2C_2 + s\left(R_1C_1 + R_2C_2 + R_2C_1\right) + 1}{s^2R_1C_1R_2C_2 + s\left(R_1C_1 + R_2C_2\right) + 1}\right)$$
$$s = i\omega, \omega = 2\pi f \tag{3}$$

We used the normalized template gamma-ray pulses in Fig. 2(e) as the input to the FDTF to determine how the "peak time" affects the shape of the output signal. Fig. 5 shows the unnormalized shape of the output signal at different peak times. As expected, a longer peak time corresponds to an increased delay of the peak timestamp of the shaped pulse.

2.3.2. FDTF optimization

The user can set the seven peak time values independently for the LG and HG paths, corresponding to 49 different combinations. For every combination of LG and HG peak times, we input the template pulses, shown in Fig. 2(e), to the LG and HG transfer functions, calculated the LG and HG peak heights, and finally calculated the PSD parameter, which is the ratio between the HG and LG output signals. The combination of peak times that yielded the largest difference between the gamma-ray and neutron PSD parameters was considered optimal for discriminating the two types of pulses and was hence selected in this study.

Table 1
Table of capacitances corresponding to the set peak time.

Peak time (ns)	C_1 (pF)	C_2 (pF)	C_3 (pF)
87.5	1.25	125	500
75	2.50	250	1000
62.5	3.75	375	1500
50	5.00	500	2000
37.5	6.25	625	2500
25	7.50	750	3000
12.5	8.75	875	3500

2.4. Experimental methods

With the optimized PSD peak times, the DS PSD method was tested using different data sets: dataset A from a pulse generator to confirm the feasibility of the method, and datasets B and C to compare the PSD performances with CI PSD. The pulse generator was used to explore a broader range of pulse shapes, and the measured data sets were used to determine the performance of the DS PSD.

2.4.1. Data sets used to test the PSD performance

The emulated pulses (dataset A) were generated using the experimental setup in Fig. 6. A DT5810B pulse generator [21] was directly connected to the A55CIT4 board. A laptop was connected to the A55CIT4 board to program the board and acquire and visualize the PSD processed data. The pulse generator created exponential pulses with a pulse shape defined by Eq. (4), where τ is the decay constant and OFFSET is 100 ns.

$$A \times \begin{cases} e^{\frac{-(t-\mathrm{OFFSET})}{\tau}} & t \geq \mathrm{OFFSET} \\ 0 & \mathrm{otherwise} \end{cases} \tag{4}$$

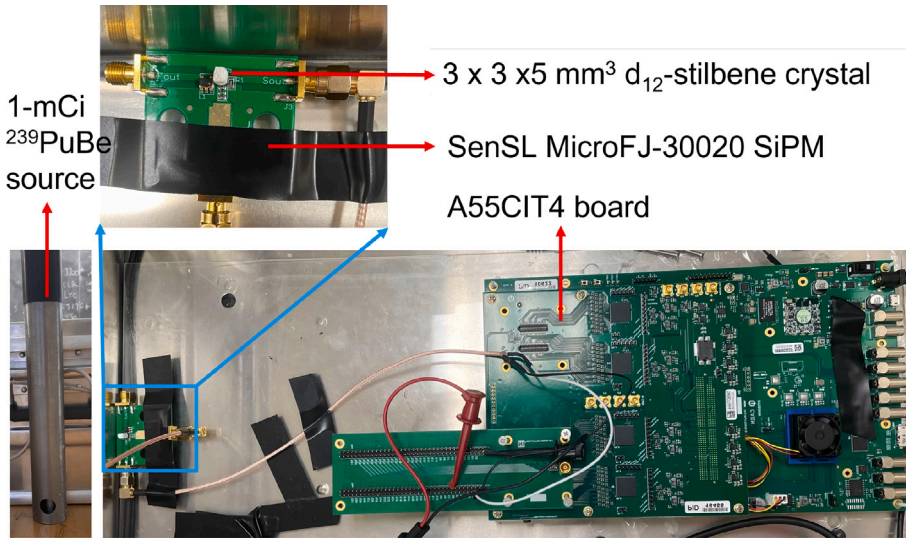

Fig. 8. Measured data experimental setup. The SiPM output is sent to the ASIC and the signal is recorded by a computer.

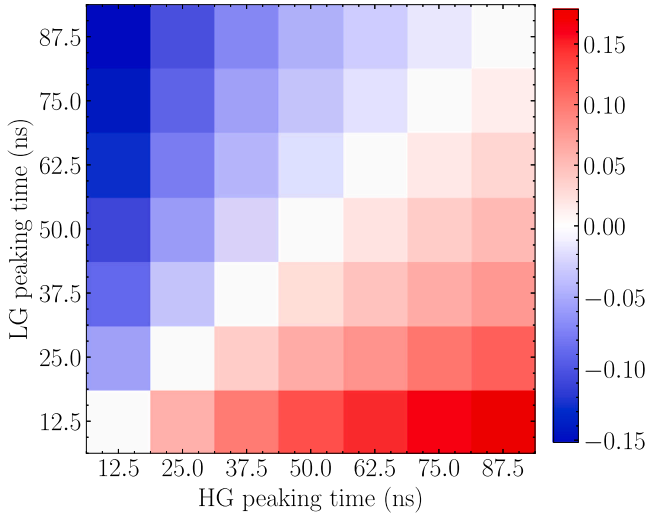

Fig. 9. $\frac{PSD_n - PSD_\gamma}{PSD_\gamma}$ as a function of LG peaking time and HG peak time. The combination of 87.5 ns for the HG peaking time and 12.5 ns for the LG peaking time, produces the largest difference between the LG and HG PSD parameters than any other combination. This is shown by the colorbar labels as the darkest red is greater than 0.15 whereas the darkest blue is exactly −0.15.

Five decay constants were tested and the pulse height was uniformly distributed between 0 and approximately 0.3 V. The shapes of the emulated pulses are shown in Fig. 7.

The experimentally measured data set (dataset C) was obtained using a $3 \times 3 \times 5$ mm^3 deuterated stilbene (stilbene-d_{12}) crystal coupled to an OnSemi MicroFJ-30020 SiPM [13]. We set the over-voltage of MicroFJ-30020 SiPM to 2 V and the max signal amplitude was 0.2 V. The signal amplitude was low enough so that no signal saturation occurred in the HG channel, and high enough so that we could still acquire low-amplitude signals in the low light output range. The setup of DS PSD is shown in Fig. 8. The SiPM signal is processed by the A55CIT4 board. To obtain dataset C, a 1-mCi^{239}PuBe source was placed at a 10 cm distance from the deuterated stilbene crystal and measured for 30 min, resulting in approximately 200,000 pulses. For comparison, we replaced the A55CIT4 board with a 14-bit 500-MSps DT5730 digitizer and performed CI PSD on the saved pulses. The data set (dataset B) acquired with the digitizer was also used for the optimization of peak times described in Section 2.3. Examples of measured pulses are shown in Fig. 2.

2.4.2. Data processing and figure-of-merit

PSD is performed on the emulated data and experimentally measured data using both the traditional charge integration method and the new PSD algorithm explained in Section 2.2. The CI gates used to calculate the total and tail areas under each pulse are 300 ns long, starting 50 ns before the trigger (pre-gate), and 220 ns long, starting 30 ns after the trigger, respectively. We varied the tail start time in the 10-50 ns range and the long gate in the 200-400 ns range and selected those gate values that resulted in the maximum PSD figure of merit (FOM), defined hereafter. The parameters for the DS-PSD were selected as described in Section 2.3.2. The results of the DS PSD were then compared with the results of the charge integration PSD. This comparison includes the PSD plots for a qualitative comparison and the calculated FOM for a quantitative comparison. The FOM is calculated by performing a double Gaussian fit of the distribution of PSD parameters using Eq. (5) and then using the parameters of the Gaussian fit as inputs to the FOM equation (Eq. (6)) [22]. μ is the mean of one peak and FWHM= $2\sqrt{2\ln 2}\sigma$ is the full-width half-maximum of the same peak. A higher FOM is preferable because it corresponds to a wider separation between the neutron and gamma ray pulses in the PSD-parameter space.

$$f(x) = a_n \exp\left(-\frac{(x-\mu_n)^2}{2\sigma_n^2}\right) + a_\gamma \exp\left(-\frac{(x-\mu_\gamma)^2}{2\sigma_\gamma^2}\right) \tag{5}$$

$$\text{FOM} = \frac{|\mu_n - \mu_\gamma|}{\text{FWHM}_n + \text{FWHM}_\gamma} \tag{6}$$

3. Results

In this section, we present the results of the optimization of the peak times based on the simulation of the circuit and the application of the DS PSD to emulated pulses as well as deuterated stilbene pulses.

3.1. FDTF optimization

We optimized the FDTF using the template pulses in Fig. 2(e) as the input. Fig. 9 shows the relative difference between neutron and gamma-ray PSD parameters for all 49 possible combinations of LG and HG peak times. The x-axis is the LG peaking time and the y-axis is the HG peaking time. Each small square is colored by the relative difference between the neutron and gamma-ray PSD parameter. The optimization showed that the difference between the LG and HG

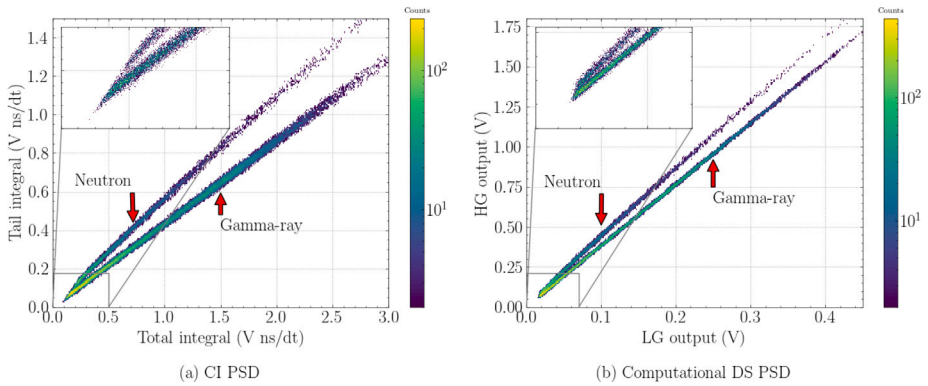

(a) CI PSD (b) Computational DS PSD

Fig. 10. Comparison of (a) charge integration PSD and (b) computational DS PSD based on dataset B acquired by measuring a ^{239}PuBe source with a stilbene-d$_{12}$ crystal.

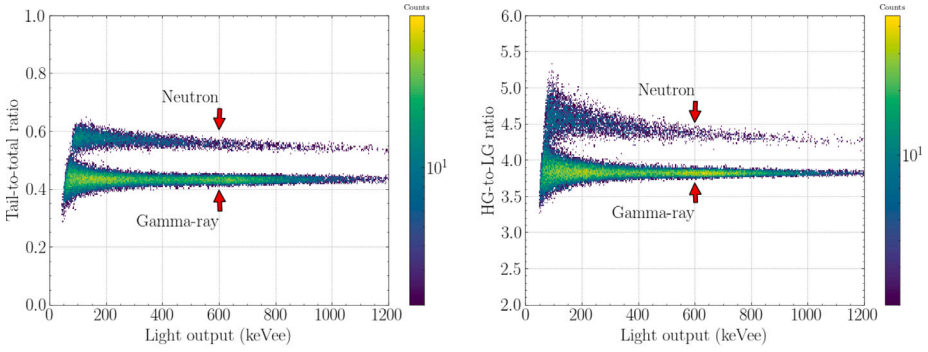

(a) CI PSD (b) Computational DS PSD

Fig. 11. Comparison of (a) charge integration PSD and (b) computational DS PSD based on dataset B acquired by measuring a ^{239}PuBe with a stilbene-d$_{12}$ crystal.

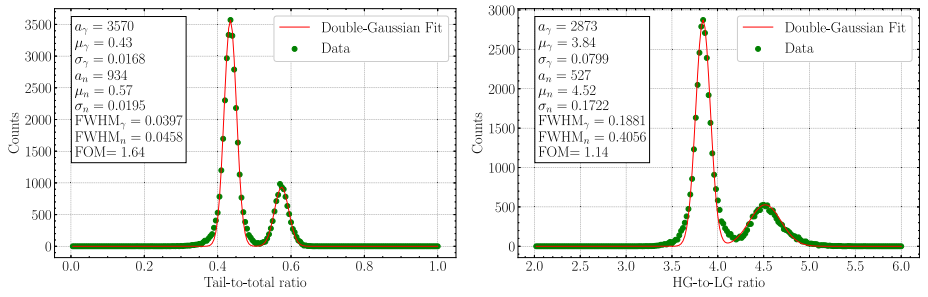

(a) CI PSD, FOM=1.64 (b) Computational DS PSD, FOM=1.14

Fig. 12. Comparison of the FOM for (a) charge integration PSD and (b) computational DS PSD based on dataset B acquired by measuring a ^{239}PuBe with a stilbene-d$_{12}$ crystal.

peaking times should be maximized in order to maximize the difference in PSD parameters. The combination that maximizes the difference between the LG and HG output values is 12.5 ns and 87.5 ns for the LG and HG peaking times, respectively. These optimized settings were used in the following experiments.

3.2. Computational implementation of DS–PSD and comparison with CI–PSD

With the optimized settings known, we can now test the performance of the DS PSD on dataset B, described in Section 2.4.1. The computational implementation of DS PSD was compared with CI PSD using dataset B and the results are shown in Figs. 10, 11, and 12. Fig. 10a shows the charge integration result, where the x-axis is the total pulse integral and the y-axis is the tail integral. Fig. 10b shows the PSD obtained with the computational DS PSD method. The x-axis is the peak height of the LG signal and the y-axis is the peak height of the HG signal. We observed a good separation between the two groups of pulses, showing the feasibility of DS PSD on this dataset. Fig. 11 shows the scatter-density PSD plots for both methods with the PSD parameter as a function of the pulse light output. Fig. 12 shows the calculated FOMs for all the pulses shown in Fig. 11, which range from 50 keVee to 1200 keVee. The feasibility of DS PSD is confirmed on measured pulses. However, the FOM is approximately 30% lower than the FOM obtained using CI PSD on the same dataset B.

3.3. On-board implementation of DS PSD and comparison with CI PSD

We used pulses from dataset A, described in Section 2.4.1, and input them to the A55CIT4-DT5550W system. We recorded the LG and HG output for each pulse and created a scatter plot of the LG output as a function of the HG output shown in Fig. 13. Each color represents one pulse type with a different time constant. The x-axis and y-axis are the LG output and HG output in ADC units, respectively. The distinct separation shows that emulated pulses with different time constants yield a different PSD parameter and can be easily discriminated.

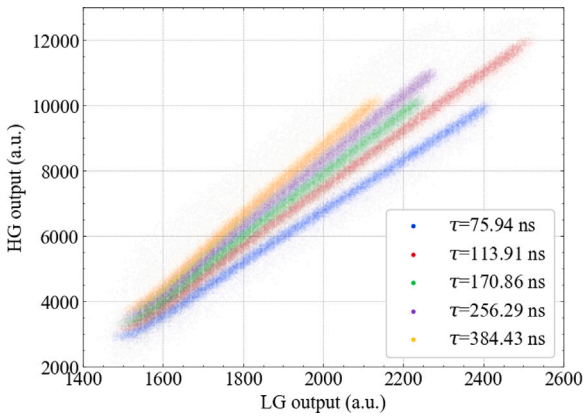

Fig. 13. DS PSD of emulated pulses (dataset A) with different time constants.

The same analysis was performed on dataset C, described in Section 2.4.1. The results of charge integration PSD (dataset B) are shown in Fig. 14a. The *x*-axis and *y*-axis are the total and tail integral, respectively. Fig. 14b shows the physical implementation of DS PSD (dataset C). The *x*-axis and *y*-axis are the LG output and HG output, respectively. Separation between the neutron and gamma-ray bands is observed, indicating that DS PSD allows us to discriminate between neutrons and gamma rays. Using the method described in Section 2.4.2, we calculated the FOM for both the DS PSD and CI PSD methods, as shown by Fig. 16. We also calculate the FOM for the first three light output bins for the CI and DS PSD methods and show the relationship between the PSD performance and light output in Fig. 17. One can observe in Fig. 17d (150–200 keVee) allows us to discriminate between gamma-ray and neutron pulses with minimum overlap between the two Gaussian distributions corresponding to these radiation types. The FOM of the DS PSD is smaller than that of the charge-integration.

4. Discussion and conclusions

An on-board ASIC-based PSD method was developed on a commercially available platform, i.e., the Citiroc1A. This DS PSD method enables the discrimination of gamma-ray and neutron pulses within a light output range of 0.1 MeVee to 2 MeVee. The presented results show that the commercially available ASIC-based readout is capable of performing on-board PSD. Unlike the traditional CI method, we used the LG and HG paths intrinsic to the Citiroc1A to extract a shape-dependent PSD parameter, defined as the ratio between the output signal of the LG and HG paths. We developed an FDFT model to emulate the response of the shaping circuit in each path and then, using the FDFT model, we optimized the PSD parameter, i.e., the peak times of the LG and HG front end. The peak times that provided the best PSD parameter are 12.5-ns for the LG path and 87.5-ns for the HG path. The optimized DS PSD performance was evaluated and compared to CI PSD using digitizer-recorded pulses. This study showed that the DS PSD is capable of discriminating gamma-ray and neutron pulses, with a FOM that is 30% lower than that of CI PSD. We then applied the DS PSD to synthetic pulses generated with a pulse emulator with controlled decay constants and confirmed experimentally that DS PSD can discriminate pulses of varying shapes. Finally, we applied the DS PSD to pulses acquired by measuring a ^{239}PuBe source with a deuterated stilbene crystal coupled to a SiPM. For this data set, the calculated FOM for DS PSD is 0.78 and 1.64 for CI PSD. The FOM for the on-board DS PSD decreased a further 20% from the computational

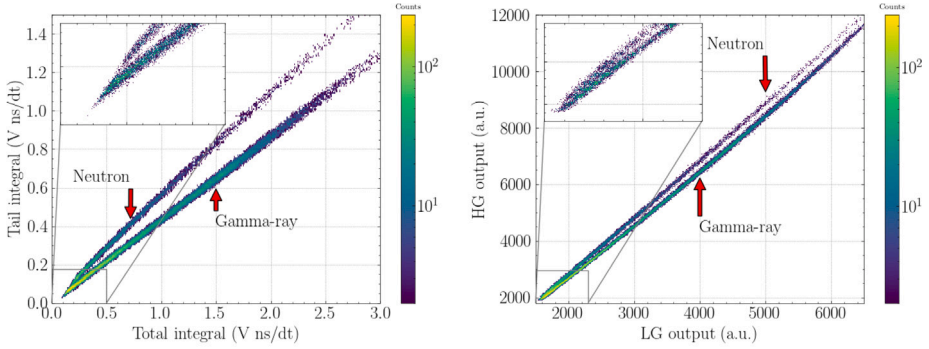

Fig. 14. Comparison of (a) charge integration PSD (dataset B) and (b) DS PSD of deuterated stilbene pulses (dataset C) acquired by measuring a ^{239}PuBe source with a stilbene-d_{12} crystal.

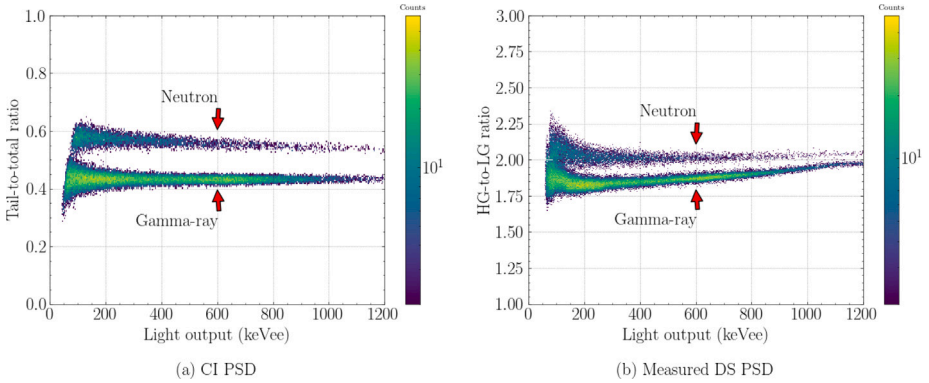

Fig. 15. Comparison of (a) charge integration PSD (dataset B) and (b) DS PSD of deuterated stilbene pulses (dataset C) acquired by measuring a ^{239}PuBe source with a stilbene-d_{12} crystal.

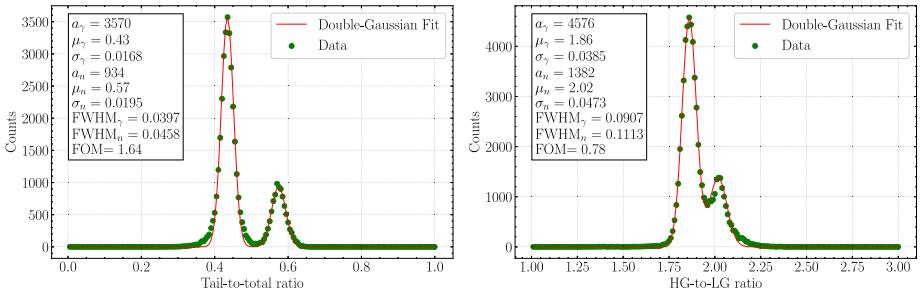

(a) CI PSD, FOM=1.64 (b) Measured DS PSD, FOM=0.78

Fig. 16. Comparison of the FOM for (a) charge integration PSD (dataset B) and (b) DS PSD (dataset C) acquired by measuring a ^{239}PuBe source with a stilbene-d$_{12}$ crystal.

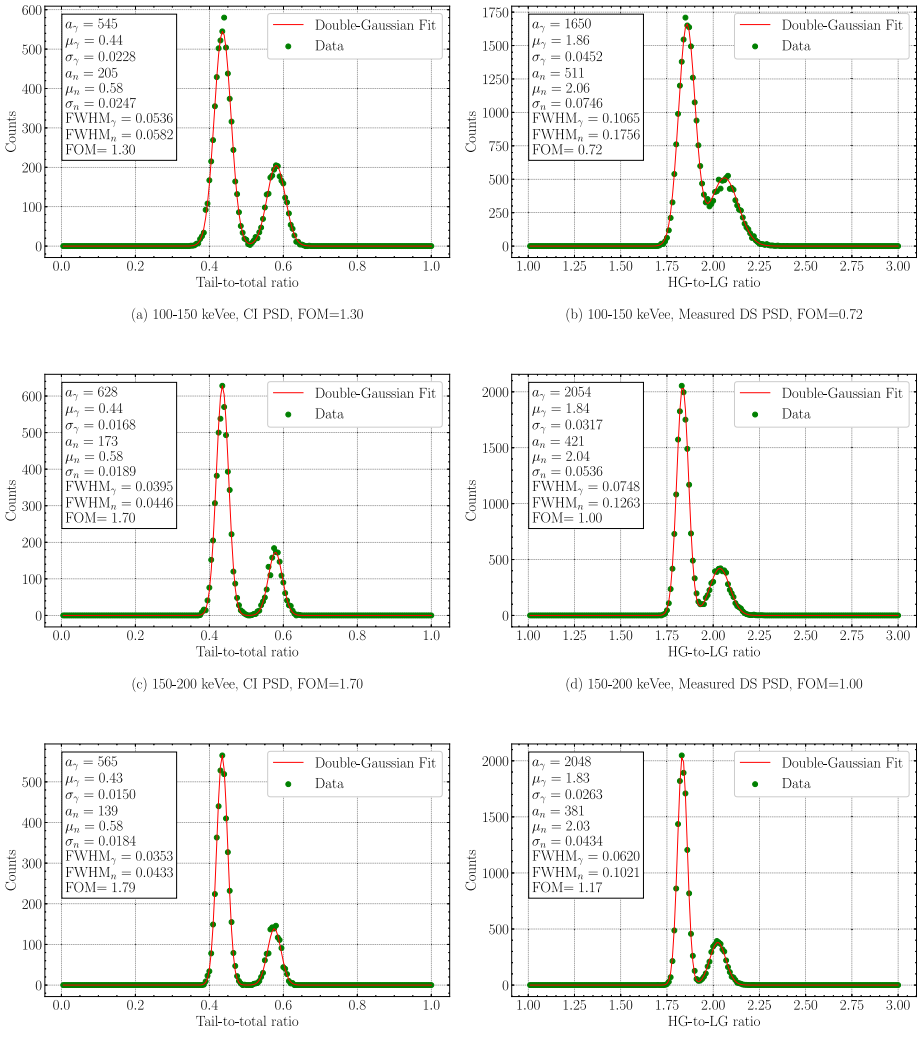

(a) 100-150 keVee, CI PSD, FOM=1.30 (b) 100-150 keVee, Measured DS PSD, FOM=0.72

(c) 150-200 keVee, CI PSD, FOM=1.70 (d) 150-200 keVee, Measured DS PSD, FOM=1.00

(e) 200-250 keVee, CI PSD, FOM=1.79 (f) 200-250 keVee, Measured DS PSD, FOM=1.17

Fig. 17. PSD performances of DS PSD (dataset C) and CI PSD (dataset B) in the first three light output bins, namely 100–150 keVee, 150–200 keVee, and 200–250 keVee.

implementation. The upwards curve in the gamma-ray band for DS PSD in Fig. 15 can be attributed to differential saturation of the LG and HG paths, which are limited to the 12.5–87.5 ns range, as the light output increases. This saturation can potentially cause the PSD parameter (HG/LG) to be overestimated thus generating an upwards trend in the gamma-ray band. Overall, CI PSD outperforms DS PSD by 50%. Out of this 50%, about 30% can be attributed to the limited number of shaping times available on the Citiroc1A. This degradation is expected and consistent with the lower FOM that DS PSD exhibits compared to CI-PSD applied to the computational analysis of measured pulses (dataset B). The remaining observed decrease in FOM for the physical implementation of the DS PSD is likely due to noise on the low gain and high gain-shaped output signals, intrinsic to the ASIC itself. Although the DS PSD performance is worse than that of CI PSD, neutron and gamma-ray pulses can be effectively discriminated at light output values higher than 0.15 MeVee, corresponding to a neutron deposited energy of approximately 0.75 MeV [23,24]. It should also be noted that DS PSD is performed on-board, in real time, and does not require the transfer of data to a separate system for further processing. The Citiroc1A in this work has a total of seven available

peak times. The DS PSD method could potentially be improved by finer tuning of the peak time, rather than selecting one of the seven options provided. In the future, we plan on testing the DS PSD performance with different realistic pulse shapes by using other organic scintillators, such as EJ-276D and small-molecule organic glass.

CRediT authorship contribution statement

John Leland: Writing – review & editing, Writing – original draft, Visualization, Software, Formal analysis, Data curation. **Ming Fang:** Writing – review & editing, Writing – original draft, Software, Methodology, Investigation, Formal analysis, Data curation. **Satwik Pani:** Writing – review & editing, Investigation, Data curation. **Yuri Venturini:** Writing – review & editing, Validation. **Marco Locatelli:** Writing – review & editing, Validation. **Angela Di Fulvio:** Writing – review & editing, Supervision, Resources, Methodology, Investigation, Funding acquisition, Formal analysis, Conceptualization.

Declaration of competing interest

The authors declare that they have no known competing financial interests or personal relationships that could have appeared to influence the work reported in this paper.

Data availability

Data will be made available on request.

Acknowledgments

This material is based upon work supported by the Department of Energy National Nuclear Security Administration, United States through the Nuclear Science and Security Consortium under Award Number DE-NA0003996.

References

[1] J.E.M. Goldsmith, M.D. Gerling, J.S. Brennan, A compact neutron scatter camera for field deployment, Rev. Sci. Instrum. 87 (8) (2016) 083307, http://dx.doi.org/10.1063/1.4961111.

[2] P.F. Bloser, J.S. Legere, S.M. Dame, M.L. McConnell, U. Bravar, J.M. Ryan, A compton telescope for remote location and identification of radioactive material, in: 2009 IEEE Conference on Technologies for Homeland Security, 2009, pp. 302–307, http://dx.doi.org/10.1109/THS.2009.5168050.

[3] J.E.M. Goldsmith, J.S. Brennan, M.D. Gerling, S.D. Kiff, N. Mascarenhas, J.L. Van De Vreugde, MINER - A mobile imager of neutrons for emergency responders, 2014, http://dx.doi.org/10.2172/1172910.

[4] J.J. Manfredi, E. Adamek, J.A. Brown, E. Brubaker, B. Cabrera-Palmer, J. Cates, R. Dorrill, A. Druetzler, J. Elam, P.L. Feng, M. Folsom, A. Galindo-Tellez, B.L. Goldblum, P. Hausladen, N. Kaneshige, K. Keefe, T.A. Laplace, J.G. Learned, A. Mane, P. Marleau, J. Mattingly, M. Mishra, A. Moustafa, J. Nattress, K. Nishimura, J. Steele, M. Sweany, K. Weinfurther, K.-P. Ziock, The single-volume scatter camera, in: A. Burger, S.A. Payne, M. Fiederle (Eds.), Hard X-Ray, Gamma-Ray, and Neutron Detector Physics XXII, Vol. 11494, SPIE, 2020, p. 114940V, http://dx.doi.org/10.1117/12.2569995.

[5] C. Piemonte, A. Gola, Overview on the main parameters and technology of modern Silicon Photomultipliers, Nucl. Instrum. Methods Phys. Res. A 926 (2019) 2–15, http://dx.doi.org/10.1016/j.nima.2018.11.119, Silicon Photomultipliers: Technology, Characterisation and Applications.

[6] L. Costrell, Development and current status of the standard nuclear instrument module (NIM) system, 1970, http://dx.doi.org/10.2172/4059108.

[7] N. Kornilov, V. Khriatchkov, M. Dunaev, A. Kagalenko, N. Semenova, V. Demenkov, A. Plompen, Neutron spectroscopy with fast waveform digitizer, Nucl. Instrum. Methods Phys. Res. A 497 (2) (2003) 467–478, http://dx.doi.org/10.1016/S0168-9002(02)01790-4.

[8] CAEN, UM7028 A55CITx CITIROC piggyback board for DT5550W, 2022, URL https://www.caen.it/support-services/documentation-area/?documentbyname=A55CIT&type=all-categories.

[9] CAEN, UM6697 DT5550W Weeroc ASICs evaluation and DAQ system, 2022, URL https://www.caen.it/products/dt5550w/.

[10] S. Kinbara, T. Kumahara, A general purpose pulse shape discriminating circuit, Nucl. Instrum. Methods 70 (2) (1969) 173–182, http://dx.doi.org/10.1016/0029-554X(69)90377-2.

[11] L. Heistek, L. van der Zwan, Pulse shape discrimination with a comparator circuit, Nucl. Instrum. Methods 80 (2) (1970) 213–216, http://dx.doi.org/10.1016/0029-554X(70)90764-0.

[12] Weeroc, CITIROC1A datasheet, 2019, URL https://www.weeroc.com/my-weeroc/download-center/citiroc-1a/89-citiroc1a-datasheet-v2-53/file.

[13] Onsemi, Silicon photomultipliers (SiPM), high PDE and timing resolution sensors in a TSV package J-series SiPM sensors, 2021, URL https://www.onsemi.com/pdf/datasheet/microj-series-d.pdf.

[14] M. Morrocchi, G. Ambrosi, M.G. Bisogni, F. Bosi, M. Boretto, P. Cerello, M. Ionica, B. Liu, F. Pennazio, M.A. Piliero, et al., Depth of interaction determination in monolithic scintillator with double side SiPM readout, EJNMMI Phys. 4 (2017) 1–25.

[15] M.L. Ruch, P. Marleau, S.A. Pozzi, Position sensitivity within a bar of stilbene coupled to silicon photomultipliers, in: 2016 IEEE Nuclear Science Symposium, Medical Imaging Conference and Room-Temperature Semiconductor Detector Workshop, NSS/MIC/RTSD, IEEE, 2016, pp. 1–3.

[16] CAEN, A7585D/DT5485P-PB digital controlled SiPM power supplies Rev.13, 2023, URL https://www.caen.it/products/a7585/.

[17] J. Birks, D. Fry, L. Costrell, K. Kandiah, The theory and practice of scintillation counting: International series of monographs in electronics and instrumentation, International Series of Monographs on Electronics and Instrumentation, Elsevier Science, 2013, URL https://www.sciencedirect.com/book/9780080104720/the-theory-and-practice-of-scintillation-counting.

[18] Y. Morishita, A. Di Fulvio, S. Clarke, K. Kearfott, S. Pozzi, Organic scintillator-based alpha/beta detector for radiological decontamination, Nucl. Instrum. Methods Phys. Res. A 935 (2019) 207–213, http://dx.doi.org/10.1016/j.nima.2019.04.024.

[19] J. Polack, M. Flaska, A. Enqvist, C. Sosa, C. Lawrence, S. Pozzi, An algorithm for charge-integration, pulse-shape discrimination and estimation of neutron/photon misclassification in organic scintillators, Nucl. Instrum. Methods Phys. Res. A 795 (2015) 253–267, http://dx.doi.org/10.1016/j.nima.2015.05.048.

[20] CAEN, A5202/DT5202 64-channel citiroc-1A unit for FERS-5200, 2023, URL https://www.caen.it/products/a5202/.

[21] CAEN, UM5312 DT5810 fast digital detector emulator user manual, 2019, URL https://www.caen.it/products/dt5810/.

[22] W.G.J. Langeveld, M.J. King, J. Kwong, D.T. Wakeford, Pulse shape discrimination algorithms, figures of merit, and gamma-rejection for liquid and solid scintillators, IEEE Trans. Nucl. Sci. 64 (7) (2017) 1801–1809, http://dx.doi.org/10.1109/TNS.2017.2681654.

[23] J. Zhou, N. Gaughan, F. Becchetti, R. Torres-Isea, M. Febbraro, N. Zaitseva, A. Di Fulvio, Light output quenching in response to deuterium-ions and alpha particles and pulse shape discrimination in deuterated trans-stilbene, Nucl. Instrum. Methods Phys. Res. A 1027 (2022) 166287.

[24] N. Gaughan, J. Zhou, F. Becchetti, R. Torres-Isea, M. Febbraro, N. Zaitseva, Y. Altmann, A. Di Fulvio, Characterization of stilbene-d12 for neutron spectroscopy without time of flight, Nucl. Instrum. Methods Phys. Res. A 1018 (2021) 165822.